Earth Surf. Dynam. Discuss., 3, 327–369, 2015
www.earth-surf-dynam-discuss.net/3/327/2015/
doi:10.5194/esurfd-3-327-2015

Earth Surface Dynamics Discussions
Open Access

The periglacial engine of mountain erosion – Part 2: Modelling large-scale landscape evolution

D. L. Egholm[1], J. L. Andersen[1], M. F. Knudsen[1], J. D. Jansen[2], and S. B. Nielsen[1]

[1]Department of Geoscience, Aarhus University, Høegh-Guldbergs Gade 2, 8000 Aarhus C, Denmark
[2]Institute of Earth and Environmental Science, University of Potsdam, Germany

Received: 30 March 2015 – Accepted: 1 April 2015 – Published: 22 April 2015

Correspondence to: D. L. Egholm (david@geo.au.dk)

Published by Copernicus Publications on behalf of the European Geosciences Union.

Abstract

An increasing number of studies point to a strong periglacial control on bedrock erosion in mountain landscapes. Periglacial processes have also been suggested to control the formation of block-fields on high-elevation, low-relief surfaces (summit flats) found in many alpine landscapes. However, to which degree periglacial processes took part in accelerating global erosion rates in response to Late Cenozoic cooling still remains as an unanswered question.

In this study, we present a landscape evolution model that incorporates two periglacial processes; frost cracking and frost creep, which both depend on the mean annual temperature (MAT) and sediment thickness. The model experiments allow us to time-integrate the contribution of periglacial processes to mountain topography over million-year time scales. It is a robust result of our experiments that periglacial frost activity leads to the formation of smooth summit flats at elevations dominated by cold climatic conditions through time periods of millions of years. Furthermore, a simplistic scaling of temperatures to δ^{18}O values through the late-Cenozoic indicates that many of the highest summit flats in mid- to high-latitude mountain ranges can have formed prior to the Quaternary. The model experiments also suggest that cooling in the Quaternary accelerated periglacial erosion by expanding the areas affected by periglacial erosion significantly. A computational experiment combining glacial and periglacial erosion furthermore suggests that landscape modifications associated with glacial activity may increase the long-term average efficiency of the frost-related processes.

1 Introduction

It is widely argued that global cooling in the late Cenozoic caused accelerated erosion of Earth's mountain landscapes (Peizhen et al., 2001; Molnar, 2004; Herman et al., 2013). This is corroborated by studies of ocean basin sedimentary records (Hay et al., 1988; Peizhen et al., 2001; Molnar, 2004), and by thermochronological studies

ESURFD
3, 327–369, 2015

of mountainous areas (Herman et al., 2013). Both sources of information point to an onset of the acceleration around 2–6 Ma ago.

The mechanisms driving this accelerated erosion are not well understood, but the increase is most clearly detected in glaciated regions, leading many to suggest that global cooling enhanced the capability of glaciers to carve valleys and cirque basins (Herman et al., 2013). The role of glaciations is backed by a close temporal correspondence between the estimated total erosion and the δ^{18}O curves that serve as a proxy for palaeo-temperature and land-ice volume (Herman et al., 2013). Other authors argue that the main driver of accelerated erosion is the increased amplitude and frequency of climatic oscillations that accompany the cooling trend (e.g. Peizhen et al., 2001; Molnar, 2004). A high level of climatic variability can lead to a situation where landscapes are rapidly readjusting to new boundary conditions and dominant erosional processes (e.g. glacial to fluvial erosion), which may result in persistently high erosion rates (Braun et al., 1999).

The notion that cold-climate processes are responsible for a large part of the increased late Cenozoic erosion is supported by the topography of mountain ranges. Most of the high mountain ranges were glaciated at some time in the Quaternary, and glaciers are thought to have reshaped landscapes significantly within a few million years (e.g. Penck, 1905; Harbor et al., 1988; Hallet et al., 1996). Fjords, U-shaped troughs, hanging valleys, and cirques represent distinct products of efficient subglacial erosion, and these landforms are now prominent in many mid- to high-latitude mountain ranges (e.g. in Norway, Greenland, New Zealand, and southern Chile). Yet, two general observations suggest that processes not directly associated with glaciers could also be of importance for the accelerated late Cenozoic erosion: (1) a large proportion of low- and mid-latitude mountain ranges have never hosted large ice masses, or bore them only briefly; and (2) global cooling over the last 15 Ma (Zachos et al., 2001) has yielded a vast areal expansion of land surface experiencing frost-driven weathering and sediment transport. Under the current warm interglacial conditions, ~ 18 % of Earth's ice-free land surface has a mean annual air temperature below 0 °C (calculated from

ESURFD
3, 327–369, 2015

data in Hijmans et al., 2005), representing a huge potential areal source of frost-driven sediment production and supply. This fact suggests that the contribution of frost-driven periglacial processes to the global sediment flux over the late Cenozoic may be notably underestimated.

Measurements of millennium-scale erosion rates (Delunel et al., 2010), as well as documented links between elevation and rock scree distribution (Hales and Roering, 2005), weathering zones (Savi et al., 2015), and threshold slopes (Scherler, 2014) suggest that frost-driven erosion can be efficient (on the order of $1\,\mathrm{mm\,a^{-1}}$) in steep mountain landscapes. Frost-related processes may therefore conceivably exert first-order control on the evolution of e.g. steep glacial headwalls and valley sides in some areas.

Cold-climate, non-glacial surface processes are also associated with the widespread areas of low-relief at high elevation known as summit flats, which are characteristic of the alpine landscapes in, for example, the Laramide ranges in the western USA (e.g. Small and Anderson, 1998; Anderson, 2002; Anderson et al., 2006; Munroe, 2006) and the Caledonian mountains in Scotland, Scandinavia, and Greenland (e.g. Rea et al., 1996; Fabel et al., 2002; Phillips et al., 2006; Nielsen et al., 2009; Goodfellow, 2012). Summit flats are typically mantled thinly with regolith that is widely held to be the product of frost-driven physical weathering (Anderson, 2002; Ballantyne, 2010; Goodfellow, 2012), although there is disagreement concerning the timing of their formation, the contribution of chemical weathering processes, and relationships to climate (Rea et al., 1996; Whalley et al., 2004; Strømsøe and Paasche, 2011; Goodfellow, 2012).

Previous studies have documented that models of regolith production and transport by frost can explain the regolith cover as well as the smooth, convex shape of the summit flats (Anderson, 2002; Anderson et al., 2012). However, substantial questions remain concerning the quantities of sediment produced and the role of these high summit flats in feeding debris to paraglacial sediment systems in the valleys below (e.g. Ballantyne, 2010). Another aspect concerning geomorphic activity is that high "accordant

ESURFD
3, 327–369, 2015

surfaces" composed of many separate summit flats at a similar elevation are frequently used as indicators of discrete tectonic uplift events (e.g. Lidmar-Bergström et al., 2000; Bonow et al., 2003, 2006; Japsen et al., 2009). The basic assumption behind this "tectonic hypothesis" is that low-relief landforms can only form at base (sea) level, and therefore the presence of low-relief topography at high elevations is best explained by vertical displacement of the landscape after it was formed (Lidmar-Bergström et al., 2013). This alternative hypothesis further motivates a better understanding of the nature of summit flats, because if low-relief landforms can develop in-situ at high elevations via frost-driven processes, this must be taken into account before uplift is inferred from topography alone.

Analysis of cosmogenic nuclide concentrations in bedrock and boulders from cold-region summit flats have revealed that (1) surface exposure ages often pre-date considerably the most recent Pleistocene glaciation, and (2) weathering processes must be very slow, with erosion rates not more than a few tens of $m\,Ma^{-1}$ (e.g. Small et al., 1997; Fabel et al., 2002; Phillips et al., 2006; Goodfellow et al., 2014). The summit flats are therefore generally considered to be slowly-evolving elements within landscapes that juxtapose deeply incised valley floors cut by Pleistocene glaciers (Small and Anderson, 1998; Anderson, 2002). But understanding the long-term topographic development of these enigmatic landforms still remains a challenge and recent studies from the Norwegian mountains suggest that, although characterized by low erosional activity during the latest glacial cycles, high-elevation, low-relief areas may have contributed notable sediment volumes to the offshore basins during the Quaternary (Steer et al., 2012). It seems that accounting for the long-term development of the summit flats requires the processes at play to be integrated throughout the Quaternary period, and possibly even further back in time because, depending on the local climate conditions, periglacial erosion may have been active several million years before glaciers were introduced into the landscapes (Nielsen et al., 2009).

The aim of this study is to time-integrate frost-driven processes and explore landscape-scale feedbacks among frost-weathering intensity, sediment mobility, and

ESURFD
3, 327–369, 2015

the evolution of relief in response to changing climate. To achieve this, we implement a frost-cracking and frost-creep model into a large-scale landscape evolution model and devise three experimental scenarios that illustrate a range of topographic and climatic boundary conditions reflecting natural landscapes: (1) a small-scale, low-relief landscape resembling an individual summit flat surface; (2) a larger-scale, high-relief landscape subject to a climate forcing that resembles late Cenozoic cooling; and (3) a large-scale landscape where periglacial and glacial erosion processes operate simultaneously.

2 The landscape evolution model

The computational landscape evolution model operates on a staggered regular grid of cells (Fig. 1). The bedrock elevation, $b(x,y)$, and the sediment thickness, $S(x,y)$, are recorded in the midpoint of each cell. The surface elevation, $h(x,y)$, of a grid cell is then

$$h(x,y) = b(x,y) + S(x,y) \tag{1}$$

We use the grid structure to model the evolution of sediment thickness and bedrock elevation over time. The term *sediment* as used here equate with regolith; that is, unconsolidated minerogenic material able to be mobilized by surface transport processes.

The continuity equation:

$$\frac{\partial S}{\partial t} = \frac{\rho_r}{\rho_s}\dot{e} - \frac{\partial qx}{\partial x} - \frac{\partial qy}{\partial y} \tag{2}$$

quantifies changes in sediment thickness over time. $\dot{e}$ is the weathering rate (the rate of bedrock conversion to sediment), $\rho_s = 2400\,\mathrm{kg\,m^{-3}}$ is the prescribed (average) density of sediment, and $\rho_r = 2900\,\mathrm{kg\,m^{-3}}$ is the density of bedrock. qx and qy represent the sediment flux along the two horizontal coordinate axes x and y. The sediment flux components are calculated at the edges between cells (Fig. 1).

ESURFD
3, 327–369, 2015

We use the frost-cracking intensity (FCI) and the sediment transport efficiency (κ) described in the companion paper (Andersen et al., 2015) to compute the weathering rate and sediment flux in every grid point:

$$\dot{e}(x,y) = k_e \mathrm{FCI}(x,y) \tag{3}$$

$$q_s(x,y) = -\kappa(x,y)\nabla h(x,y) \tag{4}$$

We assume that the weathering rate scales linearly with the frost-cracking rate, and k_e is the free scaling parameter. q_s is the sediment flux parallel to the surface in the down-slope direction. Hence, the two horizontal flux components become

$$qx = -\cos(\theta)\kappa(x,y)\frac{\partial h}{\partial x} \tag{5}$$

$$qy = -\cos(\psi)\kappa(x,y)\frac{\partial h}{\partial y} \tag{6}$$

where $\theta = \tan^{-1}(\frac{\partial h}{\partial x})$ and $\psi = \tan^{-1}(\frac{\partial h}{\partial y})$.

As documented by Andersen et al. (2015), both FCI and κ are estimated for a wide range of mean annual temperatures (MATs) and sediment thicknesses (S) (Fig. 2). Other parameters, such as the thermal properties of sediment and bedrock, the amplitudes of annual and daily temperature variations, as well as the availability of water also affect FCI and κ, but we do not pursue those issues here. We focus instead on how feedbacks between landscape evolution and frost-driven erosion operate across temporal and spatial variations in temperature and sediment thickness. In every time-step of a model simulation, we compute, by interpolation of the rates shown in Fig. 2, the FCI for each cell midpoint and κ for every cell edge using the MAT and sediment thickness, S, of the grid points. The sediment thickness of each cell is thereafter updated using explicit time integration:

$$S_i^{t+\Delta t} = S_i^t + \Delta t \frac{\rho_r}{\rho_s}\dot{e}^t - \Delta t \left[\frac{qx^t_{i,j-\frac{1}{2}} - qx^t_{i,j+\frac{1}{2}}}{\Delta x} + \frac{qy^t_{i-\frac{1}{2},j} - qy^t_{i+\frac{1}{2},j}}{\Delta y} \right] \tag{7}$$

ESURFD
3, 327–369, 2015

and the elevation of the bedrock surface is lowered by:

$$h_i^{t+\Delta t} = h_i^t - \Delta t \dot{e}^t \tag{8}$$

Due to numerical stability requirements, the explicit time integration limits the length of the time step to

$$\Delta t \leq \frac{1}{2} \frac{\min(\Delta x, \Delta y)^2}{\max(\kappa)} \tag{9}$$

where $\min(\Delta x, \Delta y)$ is the minimum grid spacing and $\max(\kappa)$ is the maximum sediment diffusivity.

In addition to this time-step constraint, the sediment flux is limited by the sediment available in the cells. While conserving the sediment volume, this constraint prevents the occurrence of negative sediment thickness values. As an example, we write the flux constraints for the size of the horizontal flux $qx_{i,j+\frac{1}{2}}$:

$$|qx|^t_{i,j+\frac{1}{2}} \leq \begin{cases} S^t_{i,j} \Delta x / \Delta t & \text{for} \quad \partial h / \partial x < 0 \\ S^t_{i,j+1} \Delta x / \Delta t & \text{for} \quad \partial h / \partial x > 0 \end{cases} \tag{10}$$

3 Computational experiments

We report the results of three types of computational experiments that all apply the expressions for frost cracking and frost creep (Fig. 2) in order to integrate erosion and sediment transport over time. The experiments are designed to explore how the combined effects of frost cracking and frost creep influence landscape evolution over several million years in the absence of other surface processes; only in the third experiment do we go beyond the periglacial system to include glacial erosion as an additional surface process. We recognise the importance of numerous other processes, such as fluvial and aeolian erosion and transport, mass wasting, and chemical weathering for

ESURFD
3, 327–369, 2015

the evolution of landscapes; however, we explicitly exclude them from our experiments. Likewise, we do not consider complicating factors such as differences in rock mass strength that arise via different lithologies and tectonic deformation histories. The objective of our experiments is to use a first-principles approach to study: (1) the topographic fingerprint of frost cracking and frost creep in relation to temperature variations that mimic those of the late Cenozoic, (2) the factors limiting long-term erosion rates, and (3) how late Cenozoic temperature shifts may have affected sediment production by frost cracking in realistic landscapes.

3.1 Experiment 1: the evolution of periglacial summit flats

The first type of experiment illustrates how the periglacial frost activity represented by Fig. 2 leads naturally to smooth parabolic areas capped by a thin sediment cover. According to Anderson (2002), this style of periglacial landscape evolution decreases local relief and establishes a steady-state landform, which thereafter is uniformly lowered by slow erosion. Through several model simulations, we first explore how weathering rate and the emergent sediment thickness depend on the climatic conditions and the free parameter k_e that scales the bedrock weathering rates.

We initiate the first landscape simulation using a fluvial-style landscape in a 2 km × 3 km grid (i.e., 100 × 150 cells with a spatial resolution of 20 m, Fig. 3a). The initial relief was generated by a landscape-evolution model based on a fluvial stream-power erosion law (Braun and Sambridge, 1997). It includes a narrow central ridge and valley structures that reach from the grid centre-line to the left and right grid boundaries. The maximum initial relief is 200 m and mean slope is 20 %, which is relatively rugged topography. The morphology of the initial relief is not of particular importance, provided that it differs from the smooth parabolic surfaces that represent the model output. We simulate frost cracking and frost creep during recurrent climate cycles that last 100 ka and entail linear MAT variations between −6 and 0 °C. For this experiment, temperature is not varied across the surface but through time only. The total simulation period is 4 Ma (i.e. 40 climate cycles). During the simulation the sediment thickness is forced to

ESURFD
3, 327–369, 2015

zero at the left and right boundaries, resembling topographic edges where the sediment from the modelled surface drops into deeper valleys. For the first simulation we set $k_e = 10^{-3}\,^{\circ}\mathrm{C}^{-1}\,\mathrm{a}^{-1}$.

During the simulation, the original topography of the surface is erased, leaving a smooth low-relief convex surface (Fig. 3). Initially, frost cracking attacks the high ridges while the associated debris accumulate in the small valleys between the ridges. Frost cracking is limited in the valleys owing to the thick sediment cover, and topographic relief drops quickly as erosion of the bedrock ridges continues (Fig. 4). After almost 4 Ma (40 climate cycles), the landscape reaches a steady state where sediment thickness (~ 3 m), relief, and surface curvature are nearly uniform across the landscape (Fig. 4). This configuration is independent of the initial topography and represents the exclusive outcome of the simulated periglacial processes. These results are in close agreement with the findings of Anderson (2002).

The relief effectively decays during the first 5–6 climate cycles (0.5–0.6 Ma). The average weathering rate also generally winds down and sediment transport gradually increases, although both are affected by the varying temperatures (Fig. 3e). After 0.6 Ma, weathering rates and sediment transport vary in a cyclic manner that mimics the change in temperature. The rates of sediment transport and frost cracking are however out-of-phase (Fig. 3e), as the cracking rate peaks during cold periods when the MAT maximizes FCI, and sediment transport is most efficient during the warmest period. This is a result of the temperature offset between the most efficient regimes of the two processes, which is $\sim -5\,^{\circ}$C for frost cracking and $\sim 0\,^{\circ}$C for frost creep (Fig. 2). Creep is thus most active when MAT approaches 0 °C, whereas frost cracking is more efficient at lower temperatures. The achievement of steady-state in the last stages of the simulation is signaled by a remarkably uniform sediment thickness (2–3 m) across the surface (Fig. 4).

ESURFD
3, 327–369, 2015

3.1.1 The influence of temperature

To investigate the influence of temperature, we repeated the simulation described in Sect. 3.1, but with climatic cycles varying within a colder temperature interval, $-12 \leq \mathrm{MAT} \leq -6\,^{\circ}\mathrm{C}$, and a warmer temperature interval, $0 \leq \mathrm{MAT} \leq 6\,^{\circ}\mathrm{C}$, respectively. Like in the first simulation, a smooth convex surface develops after a few million years in both cases (Fig. 5), but compared to that intermediate model ($-6 \leq \mathrm{MAT} \leq 0\,^{\circ}\mathrm{C}$, Fig. 5b), the colder (Fig. 5a) and the warmer (Fig. 5c) scenarios erode more slowly and produce a higher, flatter surface with less curvature. In the cold case, surface erosion is clearly limited by inefficient sediment transport: average temperature is too cold for optimal sediment transport or frost cracking, and so rates of both processes peak during the warmest interglacial periods (Fig. 5a). In the warmest scenario, frost cracking occurs mainly during the coldest periods.

The temperature dependence of frost cracking and frost creep cause the sediment cover thickness in each of these three models to undergo repeating cyclic variations in response to the climate forcing (Fig. 6). For the coldest scenario ($-12 \leq \mathrm{MAT} \leq -6\,^{\circ}\mathrm{C}$), the temperature, frost cracking, and frost creep are all in-phase, because both processes are most active when the climate is warmest. Owing to the controls on frost cracking, the sediment cover thickens slightly when temperature rises and thins when climate cools (Fig. 6). Yet, the mean sediment thickness remains relatively high because sediment creep is generally inefficient and frost cracking remain active under sediment covers up to several meters thick (Fig. 2a).

The sediment cover is much thinner for the positive MAT situation ($0 \leq \mathrm{MAT} \leq 6\,^{\circ}\mathrm{C}$) and variations through time are < 0.2 m (Fig. 6). In this case, sediment production is slow because frost cracking is impeded once a thin sediment cover has formed (Fig. 2). Still, the frost-cracking rate increases slightly when MAT approaches 1–2 °C, causing the sediment cover to grow a little during the coldest periods. Sediment creep is almost steady and independent of MAT owing to the comparatively thin cover (Figs. 2b and 5c).

ESURFD
3, 327–369, 2015

In contrast to the colder and the warmer models, the average sediment thickness varies significantly for the intermediate model ($-6 \leq \mathrm{MAT} \leq 0\,^{\circ}\mathrm{C}$). This is a result of the MAT fluctuation between those temperatures optimal for frost cracking and those optimal for frost creep. The sediment cover thickens when MAT drops below $-3\,^{\circ}\mathrm{C}$, and thins when frost creep dominates for $\mathrm{MAT} > -3\,^{\circ}\mathrm{C}$ (Fig. 6).

3.1.2 Weathering-limited versus transport-limited erosion

In the simulations presented so far, the rates of surface erosion vary between 0–$100\,\mathrm{m\,Ma^{-1}}$, with long-term average rates around 10–$20\,\mathrm{m\,Ma^{-1}}$ (Fig. 5). Two processes dictate these rates: (1) the rate of bedrock weathering by frost cracking and (2) the rate at which sediment is transported down-slope. The latter is important because the rate of frost cracking depends on sediment thickness (Fig. 2a).

Owing to a fuller understanding of the physics involved, rates of frost-creep are, however, better constrained than rates of frost cracking. As documented by Andersen et al. (2015), creep rates are calculated from modelled variations in water fraction that cause expansion and contraction of sediment during freeze-thaw events, and rates are scaled by measurable parameters, such as thermal properties and the ice-water expansion ratio. On the other hand, rates of frost-driven weathering are scaled with the frost-cracking intensity integrated throughout a year, but the scaling parameter k_e is not known. It seems intuitive that k_e should at least vary between bedrock lithologies, which may affect weathering rates through differences in, for example, tensile strength and fracture density.

To investigate the influence of k_e on the modelled weathering rates, we repeat the first experiment ($-6 < \mathrm{MAT} < 0\,^{\circ}\mathrm{C}$) several times with different values of k_e, ranging from 10^{-4} to $10^{-2}\,^{\circ}\mathrm{C}^{-1}\,\mathrm{a}^{-1}$. For each experiment we record the average weathering rate over the 4 Ma simulation period. For low values of k_e, the modelled erosion is clearly limited by the rate of frost cracking (weathering- or production-limited), and average erosion rates increase with k_e (Fig. 7). However, for higher values of k_e

ESURFD
3, 327–369, 2015

($> 0.003\,^{\circ}C^{-1}\,a^{-1}$) the average erosion rate levels out and an increase in k_e does not lead to faster erosion. At this point the erosion rate is limited by the rate of frost creep (transport-limited), which in turn is controlled by surface slope and κ (Fig. 2, Eq. 4). The curvature and average slope of the surface increase with k_e (Fig. 7), because higher levels of sediment flux are needed to evacuate the sediments produced by the relatively rapid frost cracking.

To further explore the transport-limited condition (the plateau in erosion rates obtained for high k_e values), we repeated the k_e sensitivity analysis using two higher values (4 and 6 km) for the grid width L (initially 2 km). Increasing the grid width widens the landform modelled and decreases the average surface slope. As expected, the reduced surface slope decreases the sediment flux and lowers the transport-limited erosion rates (Fig. 7).

Bedrock outcrops are persistent features of the weathering-limited condition (low k_e values). The outcrops remain along the central ridge, as tors, or along the edges of the surface where the sediment cover thins to zero. The outcrops are stable, steady-state forms that, once established, erode equally as fast as the surrounding landscape. The main difference concerns sediment thickness. While bedrock outcrops are free of sediment, the surrounds are covered to a depth of several meters, and the sediment distribution is therefore highly bimodal (Fig. 8). The frost-cracking rate is uniform in this setting due to the relation between frost cracking and sediment thickness taking the form of a "humped" function for MATs $\leq 0\,^{\circ}C$ (Fig. 2a). The humped function predicts frost cracking to be most effective under a finite thickness of sediment, with lower cracking rates accompanying both thinner and thicker sediment covers. Two different sediment thicknesses can hence lead to the same rate of frost cracking.

3.2 Experiment 2: a high-relief landscape

The second experiment illustrates the influence of frost cracking and frost creep in a larger landscape with kilometre-scale relief. For this model experiment, we use a cli-

ESURFD
3, 327–369, 2015

matic forcing resembling late Cenozoic global cooling (Fig. 9a). The climate forcing is constructed via linear transformation of a marine $\delta^{18}O$ record (Zachos et al., 2001) to sea-level temperature. So as to calibrate the temperature curve over the last 14 Ma and to approximate the first-order climate history of the North-Atlantic margins, we set the present-day sea-level MAT off southern Norway coupled with that estimated for the last glacial maximum. The resulting temperature history is inevitably a very rough estimation of the past climate; still, it enables us to incorporate the gradual cooling as well as the increasing variability of the climate throughout the late Cenozoic.

Again, we use a simulated fluvial-style initial topography with a central ridge up to 2 km high and fluvial valley structures; this time on a 25 km × 50 km grid where the left and right boundaries are at sea level (i.e. 100 × 200 cells with a spatial resolution of 250 m). The inclusion of regional isostasy incorporates the long-term effects of unloading the lithosphere by erosion. The isostatic displacements are assumed to be uniform across the grid, which, due to the flexural rigidity of the lithosphere, is a reasonable assumption for the spatial scales used here. Isostasy therefore simply raises the topography uniformly in response to the average erosion of the landscape:

$$\Delta h_{\text{isostasy}} = \frac{\rho_r \bar{e} - \rho_s \bar{S}}{\rho_a} \tag{11}$$

where $\rho_r = 2900\,\text{kg}\,\text{m}^{-3}$ is bedrock density, $\rho_s = 2400\,\text{kg}\,\text{m}^{-3}$ is sediment density, and $\rho_a = 3250\,\text{kg}\,\text{m}^{-3}$ is the density of the asthenosphere materials that provide the isostatic compensation. $\bar{e}$ is the bedrock erosion averaged across the grid, and $\bar{S}$ is the average sediment thickness. The sediment is able to escape the landscape across the left and right grid boundaries. We set $k_e = 10^{-3}\,^{\circ}\text{C}^{-1}\,\text{a}^{-1}$.

The MAT is assumed to decrease linearly with elevation at a lapse rate of $6\,^{\circ}\text{C}\,\text{km}^{-1}$, causing the highest peaks to be about 12° colder than the lowest parts of the landscape. Because of these internal temperature contrasts, the various parts of the landscape differ in response to the gradual cooling over the model simulation. The frost processes first attack the highest summits where temperatures became sufficiently low

ESURFD
3, 327–369, 2015

for frost cracking to take hold more than 10 Ma ago. Unlike the previous simulations, the initial relief is much too high to be completely erased by the frost-driven processes. However, the combined action of frost cracking and frost creep rapidly transforms the originally sharp summit crests into smooth, high-elevation summit flats in the upper parts of the landscape (Fig. 9b–e). In this experiment, the smoothing of the highest summits takes place primarily before the pronounced cooling in the Quaternary, but the same smoothing effects then spread to lower elevation summits after the onset of the Quaternary about 3 Ma ago.

The average erosion rate across the landscape increases throughout the late Cenozoic simulation period, from an initial ~ 2 to about 6 m Ma^{-1}, which represents a Pleistocene average, and reaching ~ 10 m Ma^{-1} during the coldest periods (Fig. 10a). Within this overall trend, however, we note marked differences between the high and the low parts of the landscape. At low elevations the erosion rate increases dramatically in the latest and coldest part of the Cenozoic (red curve in Fig. 10c), whereas the high-elevation summits experience stagnating or even decreasing erosion rates in the late Quaternary (green curve in Fig. 10c).

Frost-driven processes erode up to 300 m from the highest peaks over the 14 Ma simulation period, whereas $\sim$ 100–200 m is removed from the lower summits around 1000 m above sea level (Fig. 9). Slope inclinations on and near summits generally decrease in line with the process of flattening at high elevations. The total isostatic rock uplift amounts to 32 m, thereby only areas that erode less than 32 m experience a net surface uplift due to isostasy.

3.3 Experiment 3: the influence of alpine glaciations

In the final experiment, we repeat the previous simulation, but include alpine glaciations over the final 3 Ma of the simulation. Our goal is to explore how major modifications of the landscape by glacial erosion influence the overall efficiency of frost cracking and frost creep. To form the ice, we apply a simple mass-balance function that relates the

ESURFD
3, 327–369, 2015

rate of ice accumulation/ablation, $\dot{m}$, to temperature:

$$\dot{m} = \begin{cases} -\alpha\,(\mathrm{MAT} - T_{\mathrm{ELA}}) & \text{for} \quad \mathrm{MAT} < T_{\mathrm{ELA}} \\ -\beta\,(\mathrm{MAT} - T_{\mathrm{ELA}}) & \text{for} \quad \mathrm{MAT} > T_{\mathrm{ELA}} \end{cases} \tag{12}$$

where $T_{\mathrm{ELA}} = -2\,^{\circ}\mathrm{C}$ is the temperature at the equilibrium line altitude (ELA) where ablation balances accumulation; $\alpha = 0.5\,\mathrm{m\,a^{-1}\,^{\circ}C^{-1}}$ is the accumulation gradient; $\beta = 1.5\,\mathrm{m\,a^{-1}\,^{\circ}C^{-1}}$ is the ablation gradient. As before, MAT decreases linearly with elevation at a lapse rate of $6\,^{\circ}\mathrm{C\,km^{-1}}$. After $\dot{m}$ is calculated for each cell, the ice accumulation is modified to account for avalanches and snow drift (Egholm et al., 2012).

We use the iSOSIA ice model (Egholm et al., 2011, 2012) to compute the flow of ice over the final 3 Ma of the simulation. iSOSIA is a depth-integrated model that computes depth-averaged horizontal velocities and basal-sliding rates of ice. The depth-integration aids computational efficiency and enables us to model ice flow over 3 million years with time steps down to a few days. iSOSIA includes longitudinal and transverse stress components, which grant improved accuracy over standard shallow-ice approximations in steep and rugged terrain – where ice-flow velocity varies over short distances – but require iterative loops to solve the non-linear relations between stress and ice-flow velocity. Subglacial erosion rate is assumed to scale with the rate of basal sliding, which occurs only where the temperature at the ice bed is at the pressure melting point. Consequently, subglacial erosion does not occur where the ice is cold-based. The subglacial thermal state is largely a function of surface air temperature and therefore shifts through time reflecting variations in climate.

The reader is referred to Egholm et al. (2011, 2012) for further details on the ice-flow model. The important point here, however, is that the ice model is designed to produce the following behaviour, which we consider as model input: (1) The extent of the glaciers vary through time according to the climatic forcing. (2) Subglacial erosion lowers the valley floors where the ice is warm based, and this increases the relief, steepens the valley sides, and accelerates isostatic uplift. (3) The ice is allowed to transport subglacial sediment where the ice is sliding, and this effectively removes

ESURFD
3, 327–369, 2015

sediment covers in glaciated valleys over time scales of 10^4 years. (4) An ice cover thicker than 20 m prevents frost cracking from occurring, because daily and annual temperature variations in the bedrock are dampened by the overlying ice. (5) Subglacial erosion and sediment transport do not occur where the ice is cold based.

The simulated landscape is significantly modified by the inclusion of glaciers (Fig. 11). Almost the entire landscape is covered by ice masses during the coldest glaciations, whereas warmer interglacials are without ice or support only small cirque-type glaciers high in the landscape. Deep and relatively wide glacial troughs develop in the lower parts of the largest catchments; the troughs are over-deepened down to 500 m below sea level. The smaller catchments become hanging valleys.

The summit flats are notably unaffected by the subglacial erosion. Where they occur close to valley troughs, some lowering and steepening is evident, but the summit flats and their sediment covers are otherwise stable. This behaviour is not surprising as it stems directly from the prescribed accumulation patterns that minimize ice growth on convex summit flats and when ice does grow over summit flats it is cold-based and therefore non-erosive.

It is thus more interesting to note the indirect consequences of the subglacial erosion for the rates of frost cracking. The glaciers influence the conditions for frost cracking in several ways: (1) The presence of glaciers stalls frost cracking because daily and annual temperature variations are strongly dampened by the ice cover. (2) The warm-based glaciers work to strip the landscape of sediment and this may increase frost cracking upon deglaciation where frost cracking is otherwise transport limited. (3) The subglacial erosion steepens the valley sides, and the higher surface slopes boost sediment transport rates and therefore also transport-limited frost cracking. (4) Although focussed in the valleys, the average subglacial erosion is substantial and the isostatic response amounts to more than 150 m in this experiment. The slow shift in elevation causes less frost cracking at the highest summit flats where the MATs are already lower than those optimal for efficient frost cracking, and more frost cracking at lower surfaces where a further cooling due to isostasy elevates the rates of cracking.

ESURFD
3, 327–369, 2015

The positive implications of subglacial erosion for the periglacial processes are by far the strongest in our experiment: average periglacial erosion rates accelerate markedly in response to the glaciations (Fig. 12a). It is first of all the glacially steepened valley sides that experience enhanced frost cracking, shortly following deglaciation when freshly scoured glacial valleys are without sediment cover (Fig. 12b). Sediment transport is effective along the steepened valley sides, and their rates of frost-cracking are persistently high during the interglacial periods. In comparison with experiment 2, we note that inclusion of mountain glaciers results in intensified periglacial erosion along steepened valley sides (up to 400 m) and slightly less (~ 30 m) erosion of the highest summit flats (Fig. 12d).

4 Discussion

The computational experiments presented here integrate rates of periglacial frost-cracking (weathering) and frost sediment creep over millions of years and predict landscape evolution based on these processes. The weathering rates are estimated from thermal models that quantify frost-cracking intensity in bedrock based on temperatures, thermal gradients, and the availability of liquid water (Walder and Hallet, 1985; Hales and Roering, 2007; Matsuoka, 2008; Anderson et al., 2012). Likewise, the thermal models are used to predict rates of frost creep by integrating the frost-heave activity in sediments on annual time scales (Andersen et al., 2015). As demonstrated by our three experiments, periglacial activity primarily leads to high-elevation summit flats mantled with a veneer of sediment. These smoothly convex surfaces, which we suggest are analogous to cold-region blockfields, or felsenmeer (Ballantyne, 2010), are emergent properties of periglacial surface processes, as shown by previous studies (Anderson, 2002; Anderson et al., 2012). In some of our model scenarios the rise of bedrock outcrops (tors) denotes weathering-limited conditions where sediment transport matches, or exceeds, the tempo of bedrock weathering (Fig. 7). In such settings, a bimodal arrangement develops in which bare bedrock is flanked by sediment mantles 2–3 m

ESURFD
3, 327–369, 2015

thick (Fig. 8). The bimodal sediment distribution is enhanced by the humped weathering function in cold settings (MAT < 0 °C), wherein weathering rates are maximized beneath a ~ 2 m sediment cover and decline with either thinning or thickening (Fig. 2a).

A key aspect of summit flat dynamics is the coupled nature of sediment production and transport. Where bedrock weathering rates increase (via higher k_e values in our model), the system quickly becomes transport-limited as bedrock weathering near stalls once the cover exceeds about 3 m thickness (Fig. 2a). This feedback reflects the presence of water-saturated sediment that impedes the penetration of diurnal/annual temperature variations into the bedrock; an effect enhanced by latent heat in the sediment. Our results suggest that transport via frost creep limits long-term frost-weathering rates to $< 10\,\mathrm{m\,Ma^{-1}}$ for landscapes with low to moderate slopes. Such denudation rates are very low, but in good agreement with those estimated via cosmogenic nuclide measurements on cold-region blockfield/summit flats (Small et al., 1997, 1999; Goodfellow, 2012). In our model, the mode of sediment transport was restricted to frost creep so we could explore its effectiveness in isolation; however, the predominance of transport-limited conditions on summit flats implies that erosion rates might be potentially higher if other sediment transport mechanisms were accommodated, such as stream flow, subglacial activity, wind erosion, bioturbation, or other periglacial processes, such as solifluction. The transport-limited nature of the erosion may also explain why frost cracking shows much greater efficiency (rates $\sim 1\,\mathrm{mm\,a^{-1}}$) in steeper, tectonically-active landscapes where thick mantles do not develop or persist in the long-term (Hales and Roering, 2009; Delunel et al., 2010).

4.1 Assumptions and limitations

The simulated landscape evolution is a direct consequence of the theoretical and empirical assumptions in our model. We have employed the latest understanding of the physical principles that underpin large-scale periglacial landscape evolution (Hales and Roering, 2007; Anderson et al., 2012); however, many different assumptions could be

ESURFD
3, 327–369, 2015

made, which would perhaps lead to different results. In the following we attempt to outline some of the main limitations of our approach.

4.1.1 Substrate factors

The parameterization of frost creep depends on the ability of the bulk sediment to expand when freezing and contract when thawing. This process is thought to be boosted by the presence of densely packed fine-grained sediment with fully water-saturated pore spaces (Chamberlain, 1981). Yet, frost weathering itself has not been directly linked to the production of large amounts of silt-sized particles, and other mechanisms might be necessary to supply fine-grained materials. On the other hand, frost-related processes not included in our model are known to produce ample fine grains (Woronko and Hoch, 2011), and although such processes may not operate under strictly equivalent temperatures, they are likely to be active within the same temperature range. One likely contributor to rock breakdown is chemical weathering, which recent studies suggest has been underestimated in cold environments (Hall et al., 2002; Goodfellow, 2012). Indeed, the rather slow rates of frost-cracking ($\sim 10\,\mathrm{m\,Ma^{-1}}$) on high-elevation summit flats predicted by our model opens the possibility for other weathering processes to be equally fast. We note that the abundance of fine-grained material observed on many summit flats today (e.g. Strømsøe and Paasche, 2011; Goodfellow, 2012) might indicate that multiple modes of frost-driven sediment production and/or chemical weathering are keeping pace with frost cracking under current conditions. However, due to the long time scales involved, it is not straightforward to deduce a general case. The existence of fine-grained sediment might also be the result of declining frost-cracking activity, or, alternatively, the accession of allochtonous materials via glaciers or wind (Goodfellow et al., 2014).

Rock types clearly differ in their susceptibility to frost cracking (Lautridou and Ozouf, 1982; Hallet et al., 1991; Matsuoka, 2001) and although the model disregards this issue our results imply that lithology will be important for periglacial landscape evolution (Goodfellow et al., 2014). The potential for water to migrate towards incipient

ESURFD
3, 327–369, 2015

ice lenses first of all requires some degree of bedrock permeability; frost cracking thus depends on pre-existing fractures in addition to bedrock porosity. In summarizing the results of frost-cracking experiments with various rock types, Matsuoka (2001) reports frost cracking for high-porosity rocks (tuff, shale, chalk) from −5 to 0 °C, and for medium-porosity rocks (limestone, sandstones) between −6 and −3 °C. Low-porosity bedrock, on the other hand, show little or no cracking even under optimal moisture conditions (Matsuoka, 2001). Together, these observations indicate that frost susceptibility may be highly lithology-dependent and therefore should be taken into account when studying second-order feedbacks between frost action and mountain topography. The simplest way to incorporate lithological differences in our model would be to vary k_e between grid cells in the simulated landscape.

4.1.2 Water availability

Moisture is often present in mountain environments, but in certain cases precipitation may be more important than temperature for limiting frost action (Sass, 2005; Hall and Thorn, 2011). Hyper-arid regions, for instance, are too dry to promote frost cracking (Hall et al., 2002) and polar deserts sustain the slowest denudation rates on Earth (Portenga and Bierman, 2011). In less extreme environments it is worth noting that water need not be present all year to promote frost cracking operates. For negative MAT environments, water must be available at the surface in warm periods, e.g. during spring when surface warming drives snow melt or during summer when precipitation falls as rain. For positive MAT (periglacial) environments, water must be present during winter at depth within the bedrock when the surface temperature drops into the frost-cracking window. This is anticipated to apply in areas where autumn/winter is wet, or where the bedrock is prevented from drying out due to low insolation or local topographic factors.

Quantitative measurements of rock moisture in natural environments are scarce and mainly refer to steep rock faces with little or no sediment cover. Existing data point to quite consistent moisture levels at depths of a few decimeters (Sass, 2005). The ob-

ESURFD
3, 327–369, 2015

servations generally highlight the importance of direct precipitation and local climatic properties, such as prevailing wind direction, insolation patterns, and the distribution of snow, but it is doubtful that such findings apply to regolith-mantled bedrock. Our model experiments assume total water saturation in both bedrock and sediment at all times, without fluctuation. This assumption probably yields an overestimation of frost action. Yet, we note that an overall reduction in process rates will not significantly alter model outcomes, but only affect predicted erosion rates and thus the time-scale of landscape change. Prevailing wind direction and insolation patterns can, on the other hand, have an aspect-dependent influence on periglacial processes, leading to asymmetrical denudation patterns (Anderson et al., 2012). Our model simulations do not include such factors.

4.2 The development of summit flats

There are thus many aspects of periglacial processes that our landscape evolution simulations do not address directly. However, the emergence of flattish or gently convex areas (summit flats) represents a robust and highly reproducible product of all our experiments. In fact, the low-relief surfaces are characteristic of all types of transport-limited weathering, irrespective of climate. They follow from diffusive, slope-dependent transport, weathering processes that are a function of sediment thickness, and the absence of a channel (advective) network. Once sediment cover is present via whichever formation process: frost cracking, chemical weathering, or aeolian accession, the transport dynamics differ little and operate according to the diffusion-like mechanics in the model. Regolith-mantled summit flats therefore seem to arise as an inevitable consequence of long-term transport-limited behaviour on hillslopes.

A distinguishing attribute of the periglacial environment lies in the strong temperature dependence of frost cracking, which focuses weathering and erosion at particular elevation intervals. When such processes are coupled with slow rates of denudation, frost action may be concentrated on the same portion of the landscape for a long period. The slow erosion rates on summit flats predicted by our model and corroborated

ESURFD
3, 327–369, 2015

by cosmogenic nuclide measurements suggest that pronounced summit flats develop primarily in settings where other erosional agents, especially rivers and glaciers, are subdued relative to frost action and where cold climatic conditions have prevailed over Ma timescales. These criteria are likely met in tectonically quiescent regions at medium to high latitudes.

A recent compilation of thermochronological data based on Apatite Fission Track (AFT) analysis suggests that the average rates of post-Devonian erosion in the Scandinavian mountains were less than $10\,\mathrm{m\,Ma^{-1}}$ (Medvedev and Hartz, 2015). These low rates of erosion are in agreement with average millennial-scale erosion rates based on studies of cosmogenic nuclides from many areas of the planet (Portenga and Bierman, 2011). The range of measured erosion rates confirm that average erosion rates on Earth are indeed small, with clear exceptions in actively deforming orogens (Montgomery and Brandon, 2002; Von Blanckenburg, 2005) and under fast moving glaciers (Hallet et al., 1996), and this suggests that the slow frost-driven processes simulated here could in many settings represent the primary erosion agents.

4.3 Implications for glaciated passive continental margins

We now consider the implications of the model experiments for the evolution of glaciated passive margin landscapes (e.g., in Norway and Greenland), which bear resemblance to the modeled scenarios (Figs. 9 and 11). Our results indicate the highest (coldest) summit flats were largely established prior to deep cooling in the Quaternary (Fig. 9), and such areas have now become too cold for frost-driven processes to operate effectively – even during interglacial periods. The apparently minimal present-day frost action observed on the highest summit flats in Norway (Strømsøe and Paasche, 2011) is in agreement with our model results, which predict the summit flats slowly evolving into "relict" landscapes with extremely low rates of geomorphic activity in response to climatic cooling and isostatic surface uplift.

Low-relief areas at high elevation have been traditionally interpreted as evidence for accelerated rock uplift following peneplanation at base level (Lidmar-Bergström et al.,

ESURFD
3, 327–369, 2015

2000; Japsen et al., 2009). Our experiments with cold-climate processes provide a viable alternative: low-relief areas may develop more or less in situ via mechanisms unrelated to either base-level or tectonism (Anderson, 2002; Nielsen et al., 2009; Steer et al., 2012). Whether high summit flats in the mountains of Norway and Greenland are uplifted remnants of peneplains (Lidmar-Bergström et al., 2000; Japsen et al., 2009, e.g.) or the product of long-standing topography and global cooling (Nielsen et al., 2009; Steer et al., 2012) needs further investigation. Nonetheless, diffusional, transport-limited processes can undoubtedly produce smoothly convex hillslopes (Anderson, 2002); therefore, low-relief morphology alone is insufficient evidence for invoking tectonism or for identifying remnants of fluvial landscapes formed under "preglacial" conditions (Kleman and Stroeven, 1997; Hall et al., 2013; Lidmar-Bergström et al., 2013).

The highest summit flats of the computational experiments experienced decelerating frost cracking during the Quaternary mainly due to extremely cold conditions stalling rates of sediment creep (Fig. 10c, green curve). Yet, at the same time, global cooling over the last ~ 3 Ma introduced frost action to lower elevations, which represent a larger proportion of the mountain topography. Hence, the landscape as a whole experienced significant intensification of frost activity (Fig. 10a). This trend naturally depends on the specific temperature variations, the relationship between temperature and elevation, as well as the landscape hypsometry. Still, a major areal expansion of Earth's periglacial realm suggested by our results is notably compatible with the proposed acceleration of sediment production in the late Cenozoic (Hay et al., 1988; Peizhen et al., 2001; Molnar, 2004; Herman et al., 2013). Global cooling in the late Cenozoic expanded both glacial and periglacial activity. As the final experiment shows, glacial erosion may have accelerated and renewed frost cracking by stripping transport-limited sediment cover and steepening valley slopes. Hence, we suggest that periodic shift between frost-driven erosion and subglacial erosion was potentially a key driver of the accelerated denudation observed in many high and mid-latitude mountains.

ESURFD
3, 327–369, 2015

5 Conclusions

The presented landscape evolution models integrate the action of frost cracking and frost creep over million-year time scales. The rates of cracking and creep are based on thermal models that record temperature gradients and frost-heave events in the subsurface (Andersen et al., 2015). We have devised three types of computational experiments that focus particularly on the development of high-elevation summit flats on different scales of a periglacial environment. The third experiment involves both periglacial and glacial erosion processes. The key results of the computational experiments are as follows:

1. It is a highly robust result of our model simulations that frost cracking and frost creep lead to smoothing of the relief in the landscape. This is the case for a wide range of temperatures, as long as the mean annual temperature (MAT) allows for occasional freezing below −3 °C and for occasional positive temperatures allowing water to be mobilized.

2. Owing to the climate-dependency of the periglacial processes and the atmospheric cooling at higher altitudes, the efficiency of periglacial processes are optimized in certain elevation-intervals that depend on the overall climatic development. This leads to the formation of smooth surfaces at altitudes that has experienced climatic conditions optimal for periglacial processes over long time periods. This result indicates that low-relief areas can form at high elevation due to surface processes and that flatness alone is not necessarily diagnostic of a formation history close to sea level. It is important to note that the modelled topographical smoothing takes place on time scales of millions of years, in agreement with erosion rates estimated from such settings in nature (Small et al., 1997; Fabel et al., 2002; Phillips et al., 2006; Goodfellow et al., 2014).

3. Introducing a simplistic scaling of temperature to $\delta^{18}O$ values in order to mimic the late Cenozoic climatic cooling indicates that surfaces shaped by periglacial

ESURFD
3, 327–369, 2015

processes in the Miocene and Pliocene can have experienced a declining activity through the Quaternary due to the climatic cooling. This may potentially explain the low activity observed on some of these surfaces today (e.g. Rea et al., 1996; Whalley et al., 2004; Strømsøe and Paasche, 2011; Goodfellow, 2012).

4. Models incorporating both periglacial and glacial erosion processes potentially explain the highly bi-modal nature of landscape evolution in temperate alpine settings, with glacial processes carving out deep valleys and leaving the periglacially smoothed summits behind, high and dry.

5. Although the high summit flats may have experienced slower frost-driven erosion during the coldest periods of the Quaternary, the average rates of frost cracking across a large-scale area is likely to accelerate in response to Quaternary cooling. The experiment combining glacial and periglacial erosion further suggests that subglacial erosion may have increased periglacial erosion significantly during interglacials by steepening valley sides and removing sediment covers due to warm-based subglacial sediment transport.

Author contributions. D. L. Egholm and J. L. Andersen designed the study. D. L. Egholm developed model code, performed the simulations, and produced the figures. D. L. Egholm prepared the manuscript with contributions from all co-authors.

Acknowledgements. This work was supported by the Danish Council for Independent Research. J. D. Jansen was supported by a Discovery Grant from the Australian Research Council (DP130104023).

References

Andersen, J. L., Egholm, D. L., Knudsen, M. F., Jansen, J. D., and Nielsen, S. B.: The periglacial engine of mountain erosion – Part 1: Rates of frost cracking and frost creep, Earth Surf. Dynam. Discuss., 3, 285–326, doi:10.5194/esurfd-3-285-2015, 2015. 333, 338, 344, 351, 359

Anderson, R. S.: Modeling the tor-dotted crests, bedrock edges, and parabolic profiles of high alpine surfaces of the Wind River Range, Wyoming, Geomorphology, 46, 35–58, 2002. 330, 331, 335, 336, 344, 350

Anderson, R. S., Riihimaki, C. A., Safran, E. B., and MacGregor, K. R.: Facing reality: late Cenozoic evolution of smooth peaks, hlacially ornamented valleys, and deep river gorges of Colorado's Front Range, in: Tectonics, Climate, and Landscape Evolution, edited by Willett, S. D., Hovius, N., Brandon, M. T., and Fisher, D., Geol. S. Am. S., Vol. 398, 397–418, Geological Society of America, Washington, DC, 2006. 330

Anderson, R. S., Anderson, S. P., and Tucker, G. E.: Rock damage and regolith transport by frost: an example of climate modulation of the geomorphology of the critical zone, Earth Surf. Proc. Land., 38, 299–316, doi:10.1002/esp.3330, 2012. 330, 344, 345, 348

Ballantyne, C.: A general model of autochthonous blockfield evolution, Permafrost Periglac., 21, 289–300, 2010. 330, 344

Bonow, J. M., Lidmar-Bergstroem, K., and Naeslund, J.-O.: Palaeosurfaces and major valleys in the area of the Kjoelen Mountains, southern Norway – consequences of uplift and climatic change, Norsk Geogr. Tidsskr., 57, 83–101, 2003. 331

Bonow, J. M., Lidmar-Bergström, K., and Japsen, P.: Palaeosurfaces in central West Greenland as reference for identification of tectonic movements and estimation of erosion, Global Planet. Change, 50, 161–183, 2006. 331

Braun, J. and Sambridge, M.: Modelling landscape evolution on geological time scales: a new method based on irregular spatial discretization, Basin Res., 9, 27–52, 1997. 335

Braun, J., Zwartz, D., and Tomkin, J.: A new surface-processes model combining glacial and fluvial erosion, Ann. Glaciol., 28, 282–290, 1999. 329

Chamberlain, E. J.: Frost susceptibility of soil, review of index tests, Tech. rep., DTIC Document, 1981. 346

Delunel, R., van der Beek, P. A., Carcaillet, J., Bourles, D. L., and Valla, P. G.: Frost-cracking control on catchment denudation rates: insights from in situ produced 10Be concentrations in stream sediments (Ecrins-Pelvoux massif, French Western Alps), Earth Planet. Sc. Lett., 293, 72–83, 2010. 330, 345

Egholm, D. L., Knudsen, M. F., Clark, C. D., and Lesemann, J. E.: Modeling the flow of glaciers in steep terrains: the integrated second-order shallow ice approximation (iSOSIA), J. Geophys. Res., 116, F02012, doi:10.1029/2010JF001900, 2011. 342

ESURFD
3, 327–369, 2015

Egholm, D. L., Pedersen, V. K., Knudsen, M. F., and Larsen, N. K.: Coupling the flow of ice, water, and sediment in a glacial landscape evolution model, Geomorphology, 141–142, 47–66, 2012. 342

Fabel, D., Stroeven, A. P., Harbor, J., Kleman, J., Elmore, D., and Fink, D.: Landscape preservation under Fennoscandian ice sheets determined from in situ produced ^{10}Be and ^{26}Al, Earth Planet. Sc. Lett., 201, 397–406, 2002. 330, 331, 351

Goodfellow, B.: A granulometry and secondary mineral fingerprint of chemical weathering in periglacial landscapes and its application to blockfield origins, Quaternary Sci. Rev., 57, 121–135, 2012. 330, 345, 346, 352

Goodfellow, B., Stroeven, A., Fabel, D., Fredin, O., Derron, M.-H., Bintanja, R., and Caffee, M.: Arctic-alpine blockfields in the northern Swedish Scandes: late Quaternary – not Neogene, Earth Surf. Dynam., 2, 383–401, doi:10.5194/esurf-2-383-2014, 2014. 331, 346, 351

Hales, T. C. and Roering, J. J.: Climate-controlled variations in scree production, Southern Alps, New Zealand, Geology, 33, 701–704, 2005. 330

Hales, T. and Roering, J. J.: Climatic controls on frost cracking and implications for the evolution of bedrock landscapes, J. Geophys. Res., 112, F02033, doi:10.1029/2006JF000616, 2007. 344, 345

Hales, T. and Roering, J. J.: A frost "buzzsaw" mechanism for erosion of the eastern Southern Alps, New Zealand, Geomorphology, 107, 241–253, 2009. 345

Hall, A., Ebert, K., Kleman, J., Nesje, A., and Ottesen, D.: Selective glacial erosion on the Norwegian passive margin, Geology, 41, 1203–1206, 2013. 350

Hall, K. and Thorn, C.: The historical legacy of spatial scales in freeze–thaw weathering: misrepresentation and resulting misdirection, Geomorphology, 130, 83–90, 2011. 347

Hall, K., Thorn, C. E., Matsuoka, N., and Prick, A.: Weathering in cold regions: some thoughts and perspectives, Prog. Phys. Geogr., 26, 577–603, 2002. 346, 347

Hallet, B., Walder, J., and Stubbs, C.: Weathering by segregation ice growth in microcracks at sustained subzero temperatures: verification from an experimental study using acoustic emissions, Permafrost Periglac., 2, 283–300, 1991. 346

Hallet, B., Hunter, L., and Bogen, J.: Rates of erosion and sediment evacuation by glaciers: a review of field data and their implications, Global Planet. Change, 12, 213–235, 1996. 329, 349

Harbor, J. M., Hallet, B., and Raymond, C.: A numerical model of landform development by glacial erosion, Nature, 333, 347–349, 1988. 329

ESURFD
3, 327–369, 2015

Hay, W. W., Sloan, J. L., and Wold, C. N.: Mass/age distribution and composition of sediments on the ocean floor and the global rate of sediment subduction, J. Geophys. Res.-Sol. Ea., 93, 14933–14940, 1988. 328, 350
Herman, F., Seward, D., Valla, P. G., Carter, A., Kohn, B., Willett, S. D., and Ehlers, T. A.: Worldwide acceleration of mountain erosion under a cooling climate, Nature, 504, 423–426, 2013. 328, 329, 350
Hijmans, R. J., Cameron, S., Parra, J., Jones, P., and Jarvis, A.: Very high resolution interpolated climate surfaces for global land areas, Int. J. Climatol., 25, 1965–1978, 2005.
Japsen, P., Nonow, J. M., Green, P. F., Chalmers, J. A., and Lidmar-Bergström, K.: Formation, uplift and dissection of planation surfaces at passive continental margins – a new approach, Earth Surf. Proc. Land., 34, 683–699, 2009. 331, 350
Kleman, J. and Stroeven, A.: Preglacial surface remnants and quaternary glacial regimes in northwestern Sweden, Geomorphology, 19, 33–54, 1997. 350
Lautridou, J. and Ozouf, J. C.: Experimental frost shattering 15 years of research at the Centre de Géomorphologie du CNRS, Prog. Phys. Geogr., 6, 215–232, 1982. 346
Lidmar-Bergström, K., Ollier, C., and Sulebak, J.: Landforms and uplift history of southern Norway, Global Planet. Change, 24, 211–231, 2000. 331, 349, 350
Lidmar-Bergström, K., Bonow, J. M., and Japsen, P.: Stratigraphic Landscape Analysis and geomorphological paradigms: Scandinavia as an example of Phanerozoic uplift and subsidence, Global Planet. Change, 100, 153–171, 2013. 331, 350
Matsuoka, N.: Microgelivation versus macrogelivation: towards bridging the gap between laboratory and field frost weathering, Permafrost Periglac., 12, 299–313, 2001. 346, 347
Matsuoka, N.: Frost weathering and rockwall erosion in the southeastern Swiss Alps: long-term (1994–2006) observations, Geomorphology, 99, 353–368, 2008. 344
Medvedev, S. and Hartz, E. H.: Evolution of topography of post-Devonian Scandinavia: effects and rates of erosion, Geomorphology, 231, 229–245, 2015. 349
Molnar, P.: Late Cenozoic increase in accumulation rates of terrestrial sediment: how might climate change have affected erosion rates?, Annu. Rev. Earth Planet. Sci., 32, 67–89, 2004. 328, 329, 350
Montgomery, D. R. and Brandon, M. T.: Topographic controls on erosion rates in tectonically active mountain ranges, Earth Planet. Sc. Lett., 201, 481–489, 2002. 349
Munroe, J. S.: Investigating the spatial distribution of summit flats in the Uinta Mountains of northeastern Utah, USA, Geomorphology, 75, 437–449, 2006. 330

ESURFD
3, 327–369, 2015

Nielsen, S. B., Gallagher, K., Leighton, C., Balling, N., Svenningsen, L., Jacobsen, B. H., Thomsen, E., Nielsen, O. B., Heilmann-Clausen, C., Egholm, D. L., Summerfield, M. A., Clausen, O. R., Piotrowski, J. A., Thorsen, M. R., Huuse, M., Abrahamsen, N., King, C., and Lykke-Andersen, H.: The evolution of western Scandinavian topography: a review of Neogene uplift versus the ICE (isostasy–climate–erosion) hypothesis, J. Geodynam., 47, 72–95, 2009. 330, 331, 350

Peizhen, Z., Molnar, P., and Downs, W. R.: Increased sedimentation rates and grain sizes 2–4 Myr ago due to the influence of climate change on erosion rates, Nature, 410, 891–897, 2001. 328, 329, 350

Penck, A.: Glacial features in the surface of the Alps, J. Geol., 13, 1–19, 1905. 329

Phillips, W., Hall, A. M., Mottram, R., Fifeld, K., and Sugden, D. E.: Cosmogenic ^{10}Be and ^{26}Al exposure ages of tors and erratics, Cairngorn Mountains, Scotland: timescales for the development of classical landscape of selective linear glacial erosion, Geomorphology, 73, 222–245, 2006. 330, 331, 351

Portenga, E. W. and Bierman, P. R.: Understanding Earth's eroding surface with ^{10}Be, GSA Today, 21, 2011. 347, 349

Rea, B., Whalley, W., Rainey, M., and Gordon, J.: Blockfields old or new? Evidence and implications from some plateaus in northern Norway, Geomorphology, 15, 109–121, 1996. 330, 352

Sass, O.: Rock moisture measurements: techniques, results, and implications for weathering, Earth Surf. Proc. Land., 30, 359–374, 2005. 347

Savi, S., Delunel, R., and Schlunegger, F.: Efficiency of frost-cracking processes through space and time: an example from the eastern Italian Alps, Geomorphology, 232, 248–260, doi:10.1016/j.geomorph.2015.01.009, 2015. 330

Scherler, D.: Climatic limits to headwall retreat in the Khumbu Himalaya, eastern Nepal, Geology, 42, 1019–1022, doi:10.1130/G35975.1, 2014. 330

Small, E. E. and Anderson, R. S.: Pleistocene relief production in Laramide mountain ranges, western United States, Geology, 26, 123–126, 1998. 330, 331

Small, E. E., Anderson, R. S., Repka, J. L., and Finkel, R.: Erosion rates of alpine bedrock summit surfaces deduced from in situ ^{10}Be and ^{26}Al, Earth Planet. Sc. Lett., 150, 413–425, 1997. 331, 345, 351

Small, E. E., Anderson, R. S., and Hancock, G. S.: Estimates of the rate of regolith production using ^{10}Be and ^{26}Al from an alpine hillslope, Geomorphology, 27, 131–150, 1999. 345

ESURFD
3, 327–369, 2015

Steer, P., Huismans, R. S., Valla, P. G., Gac, S., and Herman, F.: Bimodal Plio-Quaternary glacial erosion of fjords and low-relief surfaces in Scandinavia, Nat. Geosci., 5, 635–639, 2012. 331, 350

Strømsøe, J. R. and Paasche, Ø.: Weathering patterns in high-latitude regolith, J. Geophys. Res.-Earth, 116, F03021, doi:10.1029/2010JF001954, 2011. 330, 346, 349, 352

Von Blanckenburg, F.: The control mechanisms of erosion and weathering at basin scale from cosmogenic nuclides in river sediment, Earth Planet. Sc. Lett., 237, 462–479, 2005. 349

Walder, J. and Hallet, B.: A theoretical model of the fracture of rock during freezing, Geol. Soc. Am. Bull., 96, 336–346, 1985. 344

Whalley, W. B., Rea, B. R., and Rainey, M. M.: Weathering, blockfields, and fracture systems and the implications for long-term landscape formation: some evidence from Lyngen and Øksfordjøkelen areas in north Norway, Polar Geogr., 28, 93–119, 2004. 330, 352

Woronko, B. and Hoch, M.: The development of frost-weathering microstructures on sand-sized quartz grains: examples from Poland and Mongolia, Permafrost Periglac., 22, 214–227, 2011. 346

Zachos, J., Pagani, M., Sloan, L., Thomas, E., and Billups, K.: Trends, rhythms, and aberrations in global climate 65 Ma to present, Science, 292, 686–693, 2001. 329, 340

ESURFD
3, 327–369, 2015

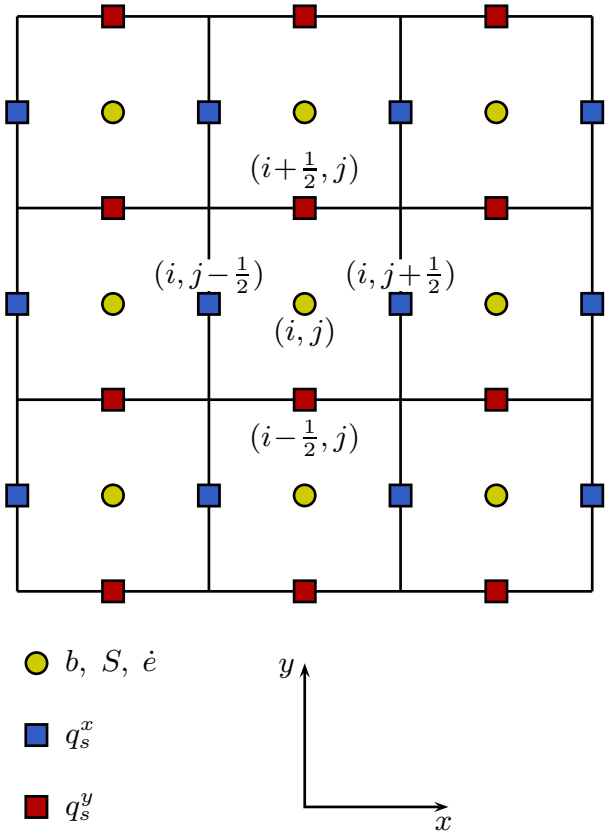

Figure 1. The landscape evolution model applies a staggered grid where the bed elevation, b, the sediment thickness, S, and the weathering rate, $\dot{e}$ are stored in cell midpoints. The horizontal sediment flux components q_s^x and q_s^y are computed at cell edges.

ESURFD
3, 327–369, 2015

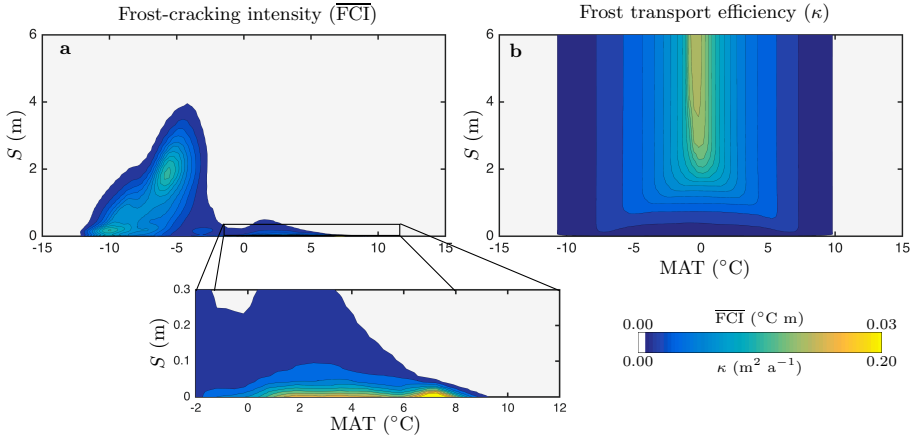

Figure 2. (a) The frost-cracking intensity ($\overline{\text{FCI}}$) and **(b)** frost sediment transport efficiency (κ) as functions of mean annual temperature (MAT) and sediment thickness (S). The contour plots are created from modelled values of frost-cracking and frost-creep for a range of combinations of MAT and S. The model behind solves the one-dimensional heat equation and integrates the rates through annual temperature cycles. The model is documented in detail in the accompanying paper (Andersen et al., 2015).

ESURFD
3, 327–369, 2015

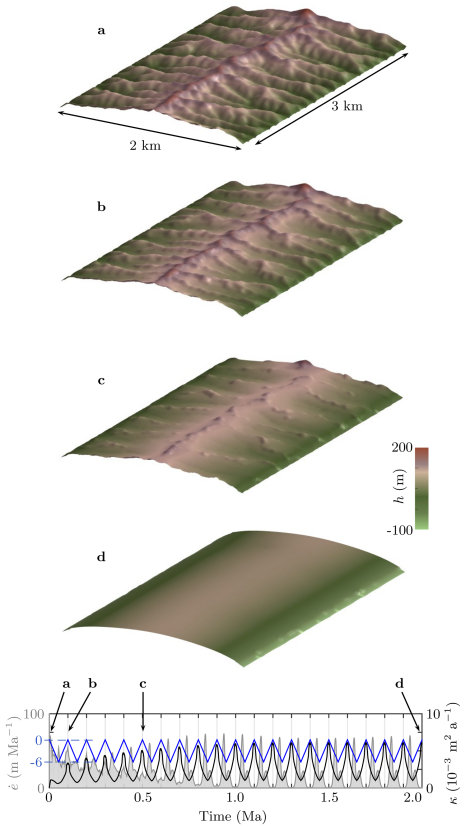

Figure 3. Computational experiment with periglacial erosion of a synthetic, fluvial-style, initial landscape. The experiment shows the development of a single summit-flat. The model landscape is exposed to 20 climate cycles that each last 100 ka and have linear saw-tooth variations in temperature. **(a)** Initial topography. **(b–d)** The predicted topography after respectively 0.1, 0.5 and 2 Ma. The bottom time series are temperature (blue), average erosion rate (gray), and average frost-creep diffusivity (black) of the modelled landscape.

ESURFD
3, 327–369, 2015

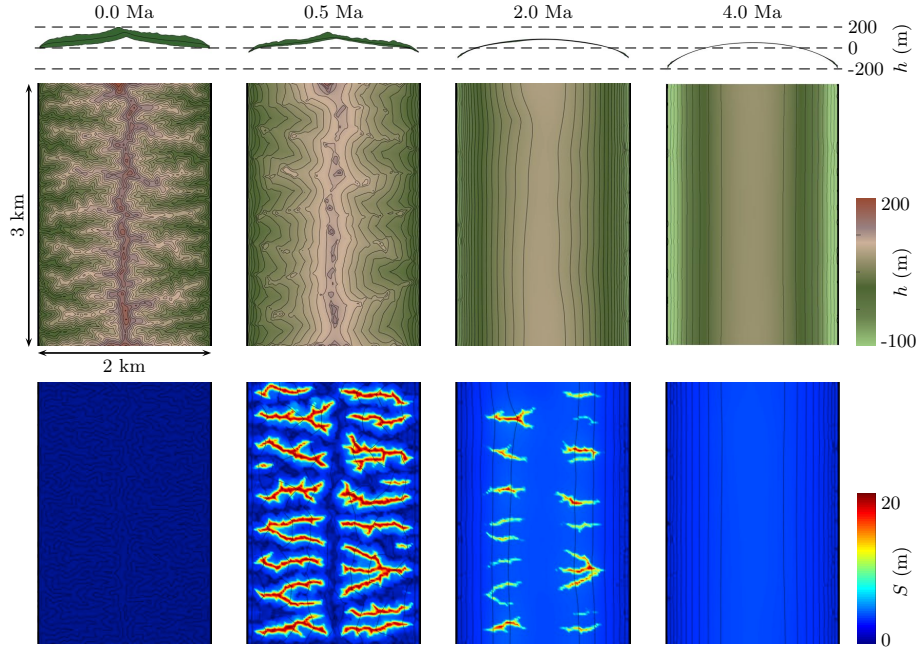

Figure 4. The same model experiment as in Fig. 3, but extended to 4 Ma and showing average relief, topography, and sediment thickness over time. The model evolution is shown at 0, 0.5, 2 and 4 Ma from left to right. Top: the topographic envelope of the landscape. The green area marks the difference between the minimum and maximum topography when measured along the long axis (3 km) of the grid. The mean topography is indicated with a black line. Note that the green area collapses over time because the initial local relief is removed by the periglacial processes. Middle: the modelled topographic development in map-view. Bottom: the distribution of sediments in the simulated landscape. Note that the initial relief decays relatively rapidly, but information on the initial relief is still preserved in the sediment distribution after 2 Ma. However, the sediment thickness becomes uniform (3–4 m) in the final stage of the simulation (4 Ma), and the modelled landscape does not have any memory of its initial configuration at this stage.

ESURFD
3, 327–369, 2015

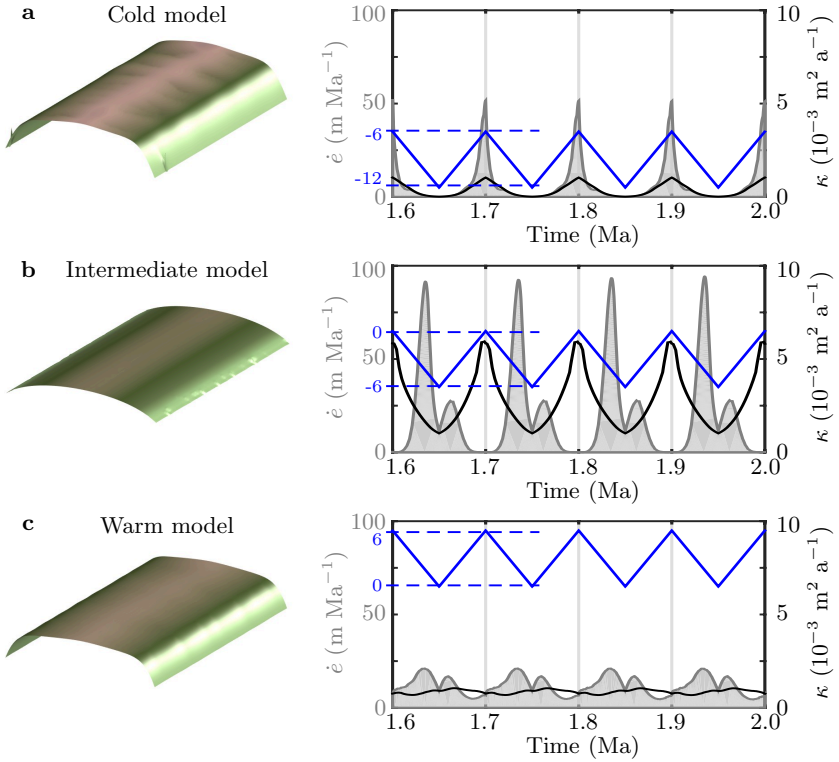

Figure 5. The development of a summit-flat under three different climatic conditions: **(a)** a cold model ($-12 < \mathrm{MAT} < -6\,^{\circ}\mathrm{C}$), **(b)** an intermediate model ($-6 < \mathrm{MAT} < 0\,^{\circ}\mathrm{C}$, same as Fig. 4), and **(c)** a warm model ($0 < \mathrm{MAT} < 6\,^{\circ}\mathrm{C}$). The final topography at 2 Ma is shown in left panels. The right panels show time-series of temperature (blue), average frost-cracking rate ($\dot{e}$, gray), and sediment diffusivity (κ, black) over four climate cycles between 1.6 and 2.0 Ma after simulation start. Note that frost-cracking and frost-creep are in-phase for the cold model, but out-of-phase for the intermediate and warm models.

ESURFD
3, 327–369, 2015

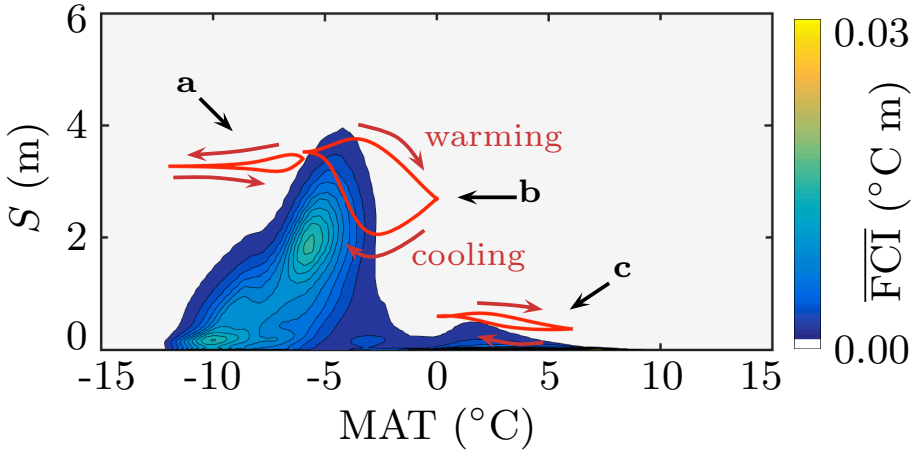

Figure 6. The evolution of mean sediment thickness (red curves) on the three summit-flats shown in Fig. 5. The rates of frost-cracking as function of MAT and sediment thickness are shown as background contours. The letters a, b and c refer to the summit-flats shown in figure 5. Note that in all three cases the mean sediment thickness varies in a cyclic manner when the MAT increase and decrease over the climate cycles. The cold and the intermediate models have much thicker sediments (~ 3 m) than the warm model (~ 0.5 m). The intermediate model shows the strongest thickening and thinning of the sediment cover because the MAT varies between the two zones of effective frost-cracking and effective frost-creep.

ESURFD
3, 327–369, 2015

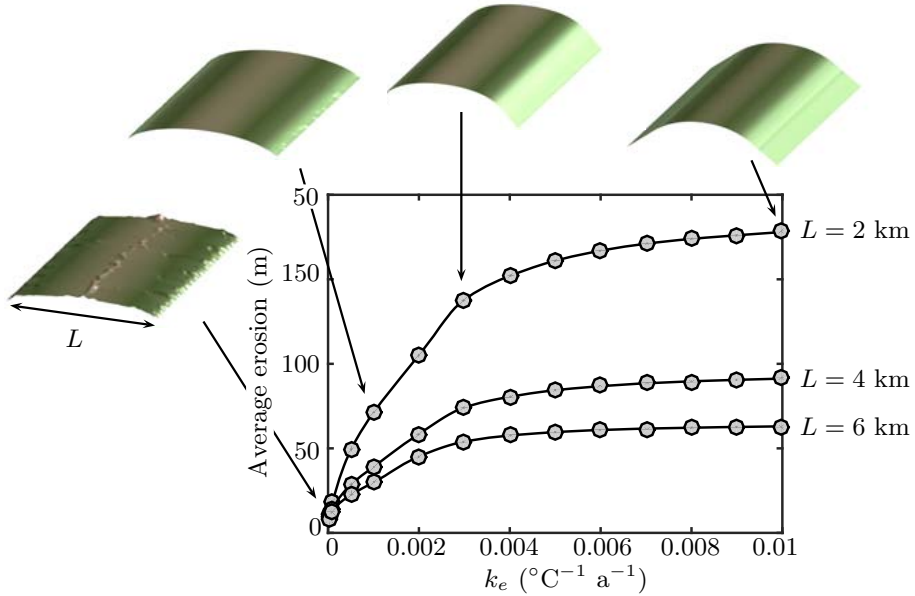

Figure 7. Mean accumulated frost-cracking after 4 Ma for different values of k_e. The results shown are for the intermediate climate model with $-6 < \mathrm{MAT} < 0\,^{\circ}\mathrm{C}$. The three curves are for model grids of different widths. The landscape is steepest for small L. Frost-cracking increases with k_e when erosion is production-limited. The three curves reach asymptotic levels for larger k_e values because erosion becomes transport-limited. The insets show some of the modelled summit-flats after 4 Ma. The curvature and slope of the summit-flats depend on the rates of erosion because slopes contribute to the scaling of sediment transport. Tors and bedrock ridges are stable phenomena in the left-most landscape where erosion is slow and production-limited.

ESURFD
3, 327–369, 2015

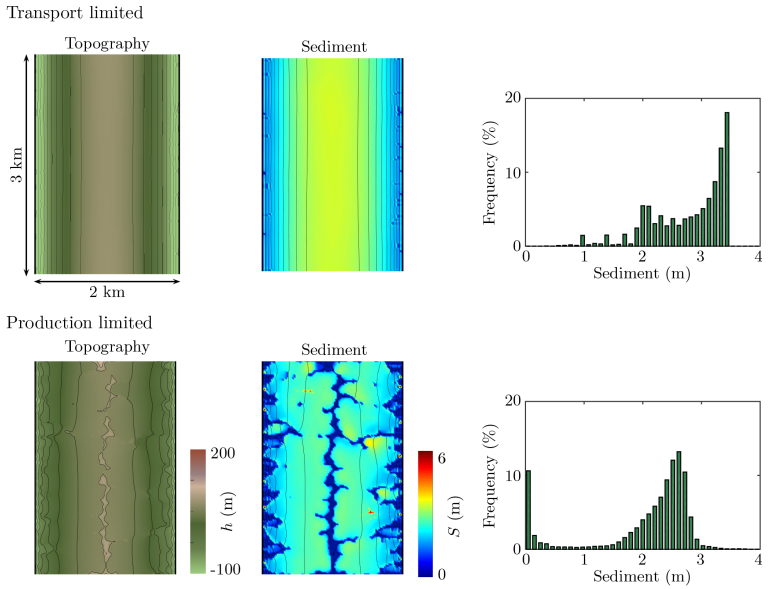

Figure 8. Results for a transport-limited (top) and a production-limited model (bottom). k_e = 0.005 °C a^{-1} for the transport-limited model and 0.0001 °C a^{-1} for the production-limited model. This is the only difference between the two model experiments, which both have $-6 <$ MAT $<$ 0 °C and L = 2 km. Left panels: modelled topography after 4 Ma. The contour spacing is 10 m. Middle panels: sediment thickness in the landscape after 4 Ma. Right panels: histogram of sediment thickness for the two cases. Almost all of the landscape has > 2 m sediment in the transport-limited case, and sediment thickness gently decreases from 3.5 m in the center to about 2 m along the edges. In contrast, the sediment distribution is highly bi-modal in the production-limited case. There is no sediment along the edges and on tors that protrude up through the sediment cover along the central ridge. In the other parts of the landscape sediment covers are mostly 2–3 m thick.

ESURFD
3, 327–369, 2015

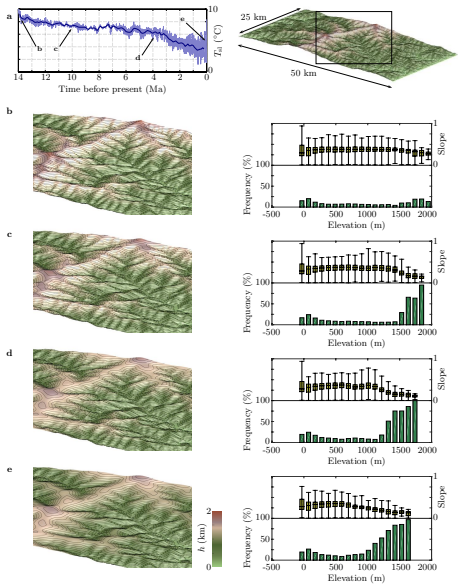

Figure 9. The second type of experiment show periglacial erosion in a landscape with kilometre-scale relief. **(a)** The 14 Ma temperature curve used as input for the model (left), and the initial topography (right). **(b–e)** Topographic evolution (left) and elevation-slope relations (right) after 0, 4, 10, and 14 Ma. To increase the level of detail, the topography is only shown for a selected region, which is outlined by the black rectangle in the right panel of **(a)**. The elevation-slope diagrams each have two sections. The upper section shows the distribution of surface slope as box-and-whisker plots for different elevation intervals. The lower section shows the frequency of flat regions (slope < 0.1) at the different elevations. Over time, the highest parts of the landscape are smoothed significantly and summit flats are formed at several levels above 1000 m. The formation of summit flats are accompanied by a distinct decrease in surface slope in the highest part of the landscape, and above 1500 m almost 100 % of the landscape has surface slopes less than 0.1. The smoothing starts at elevations above 1500 m **(c)**, but spreads to elevations above 1000 m as the climate cools **(d, e)**.

ESURFD
3, 327–369, 2015

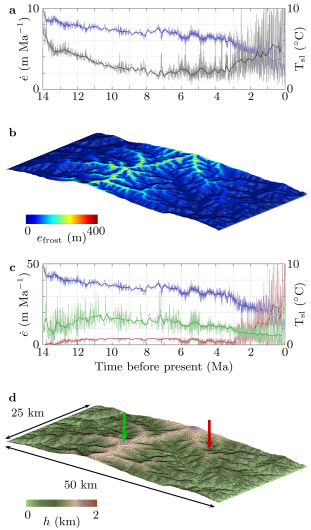

Figure 10. Erosion and erosion rates in the experiment shown in Fig. 9. **(a)** Sea-level temperature (T_{sl}, blue) and average erosion rate ($\dot{e}$, gray) throughout the 14 Ma simulation period. The erosion rates vary intensely with temperature, but the solid black line shows a smoothed average in order to highlight the overall trend. The average erosion rate decays through the first 14 Ma in response to the gradual smoothing of the summit flats. The effects of cooling takes over in the final 6 Ma of the simulations and the average erosion rate accelerate markedly as frost-cracking spreads into lower-lying regions of the landscape. **(b)** The total erosion after 14 Ma. **(c)** Erosion rates measured in the two points marked by arrows in **(d)**. Both points are at local summits, but the green point is at a higher elevation than the red and thus experience lower temperatures. The high summit has relatively high erosion rates at first, but erosion slowly stalls in the final 6 Ma of the simulation because the climate becomes too cold for efficient sediment transport by frost-creep. In contrast, the lower-lying summit (red) experiences a significant acceleration of erosion in the Quaternary.

ESURFD
3, 327–369, 2015

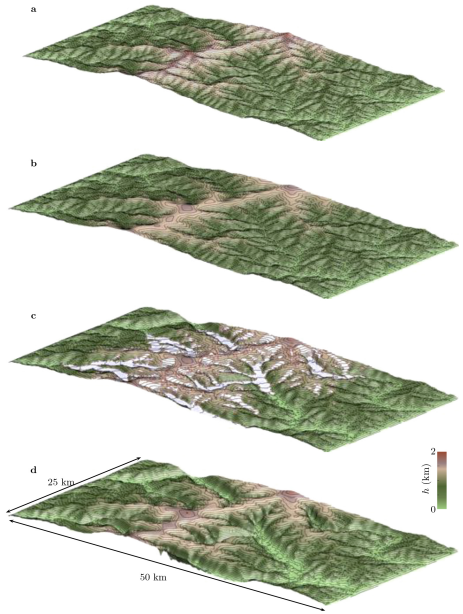

Figure 11. A combination of periglacial and subglacial erosion. The simulation is the same as in Fig. 9, but it includes glaciations within the last 3 Ma of the simulation. **(a)** The initial fluvial topography. **(b)** The modelled periglacial landscape after 11 Ma, just before glaciations start. **(c)** A snapshot of a period with glaciers (after 13.2 Ma). We note that the ice-cover varies greatly with temperature and the final 3 Ma of the simulation is dominated by glacial cycles that repeatedly cover almost the entire landscape. During the interglacials the landscape is either free of ice or includes small valley glaciers high in the landscape. **(d)** The final landscape after 14 Ma. The glaciers have carved out deep troughs that are overdeepened to about 500 m below sea-level. Smaller valleys have become hanging valleys. The summit-flats are not destroyed by the glaciers because ice is cold-based when covering the summit-flats. The final landscape is highly bi-modal, with (1) a high plateau region comprised by many summit-flats at a similar elevation, and (2) the glacial valleys that are now closer to sea-level.

ESURFD
3, 327–369, 2015

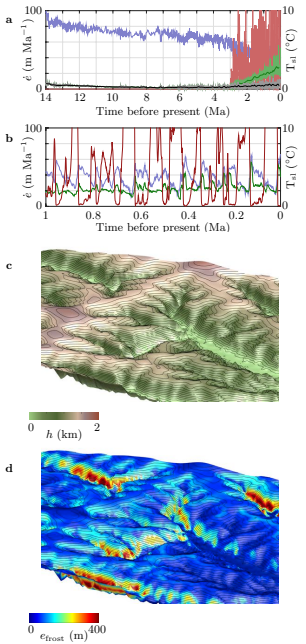

Figure 12. (a) Long-term average erosion rates in the experiment with subglacial and periglacial erosion. The experiment covers 14 Ma, but glaciations occur only during the final 3 Ma. The red curve is subglacial erosion rate, and the green curve is the periglacial erosion rate. The black curve shows the periglacial erosion rate from the experiment without glaciers (same as black curve in Fig. 10a). The blue curve is sea-level MAT. The difference between the black and green curve highlights the effect of subglacial erosion on the periglacial erosion rate, which is significantly accelerated by the glacial landscape modifications. **(b)** Details of the erosion rates during the final 1 Ma of the experiment. Red curve is subglacial erosion rate; green curve is periglacial erosion rates; blue curve is sea-level MAT. **(c)** Detail of the final stage of the landscape (same as Fig. 11d). The location of the selected area is shown by the black rectangle in Fig. 9a. **(d)** The total periglacial erosion. Note that it is primarily the glacially steepened valley sides that erode by frost cracking.

ESURFD
3, 327–369, 2015